CLIMATOLOGY

# Continuous rise of the tropopause in the Northern Hemisphere over 1980–2020

**Lingyun Meng[1,2], Jane Liu[3,4]*, David W. Tarasick[5], William J. Randel[6]*, Andrea K. Steiner[7,8,9], Hallgeir Wilhelmsen[7,8,9], Lei Wang[10,11,12], Leopold Haimberger[13]**



**Tropopause height (*H*) is a sensitive diagnostic for anthropogenic climate change. Previous studies showed increases in *H* over 1980–2000 but were inconsistent in projecting *H* trends after 2000. While *H* generally responds to temperature changes in the troposphere and stratosphere, the relative importance of these two contributions is uncertain. Here, we use radiosonde balloon observations in the Northern Hemisphere (NH) over 20°N to 80°N to reveal a continuous rise of *H* over 1980–2020. Over 2001–2020, *H* increases at 50 to 60 m/decade, which is comparable to the trend over 1980–2000. The GPS radio occultation measurements from satellites and homogenized radiosonde records are in good agreement with those results. The continuous rise of the tropopause in the NH after 2000 results primarily from tropospheric warming. A large trend in *H* remains after major natural forcings for *H* are removed, providing further observational evidence for anthropogenic climate change.**

## INTRODUCTION

The tropopause identifies the top of the troposphere and marks a separation with the stratosphere in terms of both thermal structure and chemical composition (*1*–*3*). In addition to its relevance to meteorological and chemical structures in the atmosphere, the height of the tropopause has been suggested as a sensitive indicator of anthropogenic climate change (*4*). Increases in tropopause height from the 1980s to the 1990s/2000s have been reported based on radiosonde observations (*5*, *6*), reanalysis data (*7*, *8*), and climate model simulations (*9*). Reanalyses and model simulations have suggested that the rise in the tropopause over these periods was mainly induced by tropospheric warming due to increasing greenhouse gases (GHGs) and stratospheric cooling due to stratospheric ozone depletion and increasing GHGs. However, the relative importance of tropospheric warming and stratospheric cooling remains uncertain (*4*). From radiosonde observations up to the early 2000s, a link between tropopause height increase and lower stratospheric cooling was established (*5*). However, a link between the change in tropopause height and that in tropospheric temperature was not apparent in either the extratropics or the tropics (*5*). Since the mid-1990s, cooling of the lower stratosphere has subsided owing to the successful implementation of the Montreal Protocol and its amendments (*10*–*14*). On the other hand, in the troposphere, a temporary warming slowdown appears in the early 2000s after the large El Niño of 1997–1998. This slowdown is termed the "global warming hiatus" and is widely discussed (*15*–*19*). It was found that during this period, the cooling effect from internal variability and natural forcings overwhelmed the GHG warming effect (*15*–*18*). However, as the IPO (Interdecadal Pacific Oscillation) shifted from a negative to positive phase in 2014, a combined effect of the IPO- and GHG-related forcings has since accelerated global warming (*15*, *19*–*21*). Such an evolution in tropospheric temperature since 2000 can also drive changes in tropopause height. Previously, considering changes in stratospheric cooling and tropospheric warming, some models projected a continuous increase in global tropopause height after 2000 at a rate comparable to that before 2000 (*7*, *22*), while other models projected that the rate of tropopause rise would become weaker after 2000, with a slowdown mostly in the Southern Hemisphere (SH) (*9*). Son *et al.* (*9*) compared the projection from the stratosphere-resolving chemistry climate models (CCMs) with that from the Intergovernmental Panel on Climate Change Fourth Assessment Report (AR4) models. The projections are different by hemisphere. For the Northern Hemisphere (NH), the CCMs projected that the rate of tropopause rise would slowly decrease after 2000, while the AR4 models projected a slightly larger increasing trend after 2000 than that before 2000. For the SH, both CCMs and AR4 models agreed that the tropopause would continue to rise after 2000 at a weaker rate than that before 2000, although in different magnitudes between the CCMs and AR4 models and among the CCMs. This reduction in the SH tropopause trend after 2000 was mainly attributed to stratospheric ozone recovery. In a recent numerical study (*23*), two sensitivity experiments were conducted by fixing the amount of ozone depleting substances (ODS) and GHG emissions at their 1960 levels. The results show that, on the global scale, tropopause height would continue to rise at a faster rate over 2000–2080 than before if the amount of ODS is fixed. If GHG emissions are instead fixed, the tropopause height would decrease after 2000. If all forcings are considered, the rate of tropopause rise before and after 2000 would be comparable.

In 2016, the Integrated Global Radiosonde Archive (IGRA) was updated to version 2 (IGRA2), which includes more stations and reduces more biases than the previous version. In recent decades, satellite GPS radio occultation (RO) measurements and the homogenized gridded radiosonde data have also become available. Therefore,

[1]School of Atmospheric Sciences, Nanjing University, Nanjing, China. [2]International Institute for Earth System Science, Nanjing University, Nanjing, China. [3]Department of Geography and Planning, University of Toronto, Toronto, Canada. [4]Key Laboratory for Humid Subtropical Eco-geographical Processes of the Ministry of Education, College of Geographical Sciences, Fujian Normal University, Fuzhou, China. [5]Air Quality Research Division, Environment and Climate Change Canada, Downsview, ON M3H 5T4, Canada. [6]National Center for Atmospheric Research, Boulder, CO, USA. [7]Wegener Center for Climate and Global Change, University of Graz, Graz, Austria. [8]Institute for Geophysics, Astrophysics, and Meteorology/Institute of Physics, University of Graz, Graz, Austria. [9]FWF-DK Climate Change, University of Graz, Graz, Austria. [10]Department of Atmospheric and Oceanic Sciences & Institute of Atmospheric Sciences, Fudan University, Shanghai, China. [11]Shanghai Qi Zhi Institute, Shanghai, China. [12]Big Data Institute for Carbon Emission and Environmental Pollution, Fudan University, Shanghai, China. [13]Department of Meteorology and Geophysics, University of Vienna, Wien, Austria.
*Corresponding author. Email: janejj.liu@utoronto.ca (J.L.); randel@ucar.edu (W.J.R.)

in view of the issues discussed above, this study is motivated (i) to determine the long-term (1980–2020) changes in tropopause height associated with anthropogenic activities using the updated IGRA2 and other datasets, (ii) to provide a robust assessment on the sensitivity of tropopause height to the temperature variations in the troposphere and stratosphere, and (iii) to assess the relative importance of tropospheric warming and stratospheric cooling to the change in tropopause height before and after 2000 under a combined influence of GHG emissions and stratospheric ozone changes. Specifically, we investigate the variation in tropopause height (referred as *H*; see Materials and Methods for its definition) in the NH, primarily over 20°N to 80°N, where most radiosonde stations are located (fig. S1). We compare the *H* variations in two periods before and after 2000 based on the dense radiosonde balloon observations, largely over land, from the IGRA2 data [(*24*); see Materials and Methods on how to select stations and see fig. S1 and table S1 for information of all selected stations]. We further use the GPS RO measurements over 2001–2020 (*25*) and the gridded homogenized radiosonde observations from the Radiosonde Observation Correction Using Reanalyses (RAOBCORE) data and Radiosonde Innovation Composite Homogenization (RICH) data (*26*, *27*) over 1980–2020 to compare with the IGRA2 data. We evaluate the behavior of the tropopause height changes in the NH with time and by latitude. To isolate the impact of anthropogenic activities on the tropopause, the variations related to major natural forcings, including volcanic eruptions, ENSO (El Niño–Southern Oscillation), and QBO (quasi–biennial oscillation), are statistically removed from the original time series of the IGRA2, GPS RO, RAOBCORE, and RICH data to generate natural variability–removed time series (see Materials and Methods and fig. S2 for details; all the discussion in this paper is based on the natural variability–removed time series unless stated otherwise). We evaluate the relative importance of temperature changes in the troposphere and stratosphere to the tropopause height changes through detailed comparisons with the radiosonde temperature profiles using robust statistical methods (see Materials and Methods) and thus demonstrate that the continuous rise of the tropopause in the NH after 2000 is mainly due to ongoing warming of the troposphere.

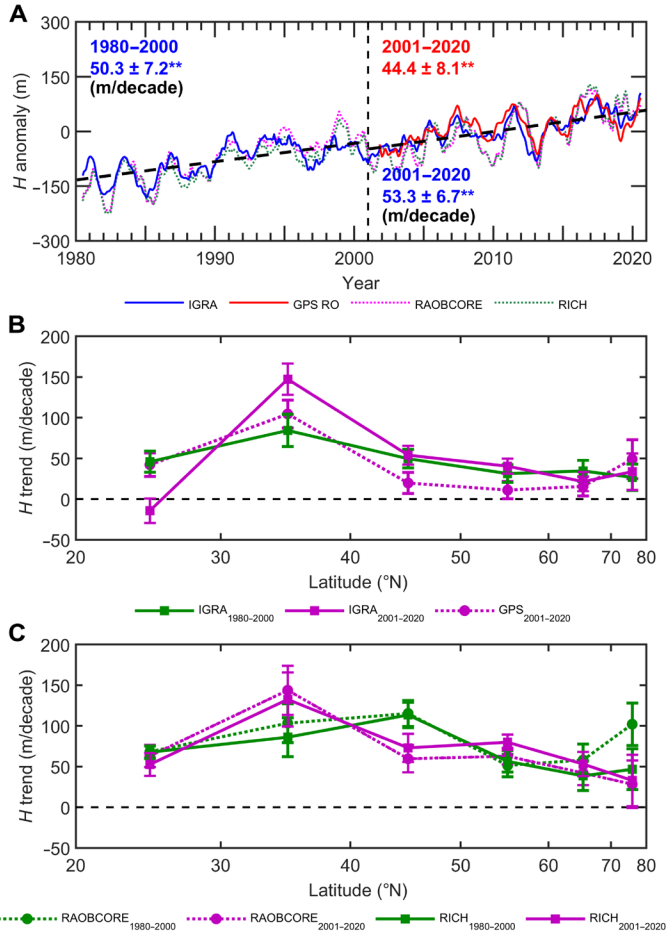


**Fig. 1. Variations in zonal mean tropopause height over the NH and derived trends from the IGRA2, RAOBCORE, and RICH data over the time period 1980–2020 and GPS RO satellite data over 2001–2020.** (**A**) Time series of deseasonalized monthly anomalies of tropopause height (*H*) from IGRA2 (solid blue line), RAOBCORE (dashed purple line), RICH (dashed green line), and GPS RO (solid red line) averaged over 20°N to 80°N. The vertical dashed black line indicates the end of 2000, dividing the study period into two subperiods (1980–2000 and 2001–2020). The dashed thick black lines denote the linear trends in IGRA2 over the corresponding periods. The values of the trends and their 95% confidence intervals in the two subperiods are denoted in blue for IGRA2 and in red for GPS RO, all statistically significant at the 95% confidence level (indicated by double asterisks). (**B**) Trends in zonal-mean *H* from IGRA2 are compared between the two subperiods (1980–2000 in solid green line and 2001–2020 in solid purple line) and also from GPS RO over 2001–2020 (dashed purple line). The *x* axis is shown on the cosine latitude scale. The error bars indicate the 95% confidence intervals for the trends. In the time series, the effects of volcanic eruptions, ENSO, and QBO have been statistically removed. (**C**) The same as (B) but for trends in zonal-mean *H* from RAOBCORE (dashed line) and RICH (solid line) over the two subperiods (1980–2000 in green and 2001–2020 in purple).

## RESULTS

### Long-term variability in tropopause height in the NH over 20°N to 80°N from 1980 to 2020

Over the entire study period from 1980 to 2020, a continuous rise of *H* in the NH over 20°N to 80°N is evident in the natural variability–removed IGRA2 radiosonde time series (Fig. 1A). Positive trends in *H* prevail in IGRA2 over most subperiods longer than 10 years (fig. S3A). Similarly, the corresponding *H* in gridded RAOBCORE or RICH data also increases monotonously with a faster rate (70 to 80 m/decade) than that in IGRA2 (50 to 60 m/decade) (Table 1A). These differences may be due to that *H* for RAOBCORE and RICH is determined based on a monthly mean temperature profile, while for IGRA2, *H* is determined based on single profiles, and the resulting *H* values are then averaged for monthly means. In addition, the vertical resolution of the RAOBCORE and RICH data is somewhat coarser than that of IGRA2 (see Materials and Methods). The correlation coefficient between the monthly anomalies of *H* in IGRA2 and RAOBCORE (or RICH) data is 0.87 (or 0.89) over 1980–2020. In the original IGRA2 data in which the signals of natural variability are not filtered out, the mean *H* increases from 12.2 km in 1980 to 12.4 km in 2020 in absolute altitude. The increasing trend in *H* over 1980–2020 is estimated to be 49.7 ± 3.6 m/decade in the original IGRA2 data and 44.0 ± 2.5 m/decade in the natural variability–removed IGRA2 data.

For the first subperiod of 1980–2000, *H* rises with a rate of 50.3 ± 7.2 m/decade in the natural variability–removed IGRA2 radiosonde data (Fig. 1A for time series and fig. S4A for spatial variation). Similar positive trends over this period were reported for the

globe (*5*) and other regions (*6*, *28*). For the second subperiod of 2001–2020, a comparable increase of *H*, 53.3 ± 6.7 m/decade is observed in IGRA2 (Fig. 1A and fig. S4B). In the same period, the trend in *H* in satellite GPS RO data is 44.4 ± 8.1 m/decade, and the monthly anomalies of *H* in GPS RO are closely correlated with those in IGRA2 [the correlation coefficient (*r*) is 0.84; similar to *H* in IGRA2, *H* in GPS RO is also calculated based on single profiles]. The *H* trends by latitude over 2001–2020 are similar to those over 1980–2000 in IGRA2 (Fig. 1B). In both IGRA2 and GPS RO, a rise of *H* over 2001–2020 prevails in all latitudinal bands with larger trends around 30°N to 40°N reaching about 100 m/decade. The maximum *H* trend around 30°N to 40°N possibly includes effects from a tropical expansion and poleward shift of the subtropical jet over the past four decades (*29*–*31*), which is associated with enhanced tropospheric warming and lower stratospheric cooling in the mid-latitudes (*14*, *29*). In RAOBCORE and RICH (Fig. 1C), the latitudinal variation in the *H* trend is more similar to that in IGRA2 over 2001–2020 than over 1980–2000. The relative differences in the *H* trends between the original and natural variability–removed time series in all datasets are less than 30% for both subperiods (Table 1), demonstrating that anthropogenic forcings are the primary drivers for the changes in *H*.

**Table 1. Trends in tropopause height (*H*), tropospheric temperature ($T_{TRO}$), and stratospheric temperature ($T_{STR}$).** The trends in *H* and their 95% confidence intervals are listed for the NH (20°N to 80°N) over 1980–2000 and 2001–2020, based on the radiosonde IGRA2, RAOBCORE, and RICH data. In addition, trends in *H* over 2001–2020 based on the GPS RO data are shown. The trends are derived from the natural variability–removed time series (A) in which the effects of volcanic eruptions, ENSO, and QBO have been statistically removed (Figs. 1 and 4) and from the original time series (B). All trends are statistically significant at the 95% confidence level.

**A. Trends in the natural variability–removed time series**

| Trend | Data source | 1980–2000 | 2001–2020 |
|---|---|---|---|
| *H* (m/decade) | IGRA2 | 50.3 ± 7.2 | 53.3 ± 6.7 |
| | GPS RO | – | 44.4 ± 8.1 |
| | RAOBCORE | 83.7 ± 7.2 | 76.9 ± 9.4 |
| | RICH | 74.0 ± 7.0 | 79.8 ± 9.9 |
| $T_{TRO}$ (K/decade) | IGRA2 | 0.17 ± 0.03 | 0.31 ± 0.02 |
| | RAOBCORE | 0.20 ± 0.03 | 0.29 ± 0.02 |
| | RICH | 0.20 ± 0.03 | 0.33 ± 0.02 |
| $T_{STR}$ (K/decade) | IGRA2 | −0.58 ± 0.05 | −0.14 ± 0.04 |
| | RAOBCORE | −0.41 ± 0.05 | −0.14 ± 0.04 |
| | RICH | −0.44 ± 0.05 | −0.10 ± 0.04 |

**B. Trends in the original time series**

| Trend | Data source | 1980–2000 | 2001–2020 |
|---|---|---|---|
| *H* (m/decade) | IGRA2 | 57.8 ± 9.8 | 58.8 ± 10.4 |
| | GPS RO | – | 56.8 ± 12.1 |
| | RAOBCORE | 102.2 ± 12.4 | 75.0 ± 10.9 |
| | RICH | 92.2 ± 12.8 | 78.4 ± 11.6 |
| $T_{TRO}$ (K/decade) | IGRA2 | 0.18 ± 0.04 | 0.34 ± 0.04 |
| | RAOBCORE | 0.22 ± 0.04 | 0.32 ± 0.04 |
| | RICH | 0.23 ± 0.04 | 0.36 ± 0.03 |
| $T_{STR}$ (K/decade) | IGRA2 | −0.72 ± 0.08 | −0.09 ± 0.06 |
| | RAOBCORE | −0.52 ± 0.07 | −0.13 ± 0.06 |
| | RICH | −0.56 ± 0.07 | −0.09 ± 0.06 |

## Responses of tropopause height to temperature variations in the troposphere and stratosphere

Variability in tropopause height is closely related to the thermal structure below and above (*5*, *8*, *32*). On the monthly scale (Fig. 2A), monthly anomalies of tropopause height are positively correlated with tropospheric temperature anomalies and negatively correlated with stratospheric temperature anomalies. Vertically, the maximum correlation coefficient between *H* and temperature ($r_{max}$) is 0.74 around 400 hPa and the minimum correlation coefficient ($r_{min}$) is −0.64 around 100 hPa, consistent with previous studies (*5*, *32*). The correlation between *H* and vertical temperature profiles on the monthly scale is similar to that on the synoptic scale presented in literature (*5*), which is linked to the balanced dynamical structure in cyclones and anticyclones (*33*). The similar vertical variations in the correlations on monthly and synoptic scales suggest that the accumulated effect of synoptic variability, in the troposphere and lower stratosphere, can influence monthly temperature variability and, in turn, modulate monthly anomalies in *H*. Quantitatively, at the altitude of $r_{max}$, the regression coefficient between *H* and tropospheric temperature averaged over the NH is ~220 m/K over 1980–2020, while at the altitude of $r_{min}$, the averaged regression coefficient between *H* and stratospheric temperature is about −170 m/K (Fig. 2B). The responses of *H* to variations in tropospheric temperature ($T_{TRO}$; see Materials and Methods for its calculation) and stratospheric temperature ($T_{STR}$; see Materials and Methods for its calculation) are further investigated on the multidecadal scale by analyzing relationships between derived trends in *H* and those in $T_{TRO}$ and $T_{STR}$ across the different stations and for different periods (see Materials and Methods). For the decadal-scale variations, we find that the trends in *H* and those in $T_{TRO}$ are positively correlated

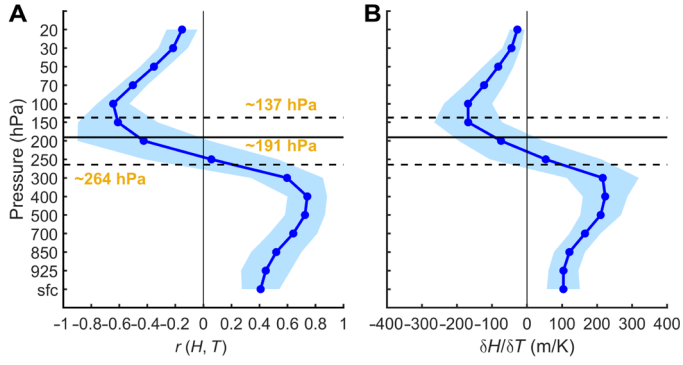


**Fig. 2. Vertical profile of the correlation between *H* and temperature at a given altitude.** (**A**) Mean correlation coefficients (*r*) between deseasonalized monthly anomalies of *H* and temperature at different altitudes in the troposphere and stratosphere over 1980–2020. The shaded area represents ±SD. Each value of *r* shown is a mean over 149 stations in the NH. The mean *H* (solid horizontal line) and its ±SD (dashed horizontal line) are also indicated. For presentation, altitudes are converted to pressures. (**B**) The same as (A) but for the vertical profile of the regression coefficients (m/K) between *H* and temperature at a given altitude. The time series of monthly anomalies used here include the signals of volcanic eruptions, ENSO, and QBO.

across the different stations and significant at the 95% level, ranging over 0.2 to 0.8 (Fig. 3A) with a mean correlation of 0.49. In contrast, the trends in $H$ and those in $T_{STR}$ are all negatively correlated, ranging from −0.6 to zero with a mean of −0.32 and most (96%) being statistically significant (Fig. 3C). To account for temporal autocorrelation, the significance of the mean $r$ between trends in $H$ and those in $T_{TRO}$ and $T_{STR}$ is tested using a bootstrap method [(*34*); see Materials and Methods]. The results indicate that both the mean $r$ values are significant at the 95% confidence level, with confidence intervals of ±0.25 for $T_{TRO}$ and ±0.19 for $T_{STR}$. Such a significant relationship between the trends in $H$ and $T_{TRO}$ (Fig. 3A) was not observed in the IGRA version 1 radiosonde data over 1980–2004 (*5*). With IGRA2, we also reveal a closer association between the trends of $H$ and of $T_{TRO}$ than that between the trends of $H$ and of $T_{STR}$ in the NH over 1980–2020, as well as over 1980–2004 [the same period as in (*5*)]. These new results may be partially due to better calibration, more station records, and longer station records in IGRA2, especially in the NH. Another reason may be related to the difference in the study domains between this study and the previous study of (*5*), as the latter considered $H$ over the entire globe, and variability in the thermal structures above and below the tropopause differs significantly with latitude (*14*, *21*). The correlation between the trends of $H$ and of $T_{STR}$ in Fig. 3C is weaker than previously reported from observations for the globe (*5*) and model simulations for the NH (*9*). In addition to the differences in radiosonde data versions and study domains between this and the previous studies discussed above, the weaker correlation in the trends of $H$ and of $T_{STR}$ from this study may also be related to the observed inflection point in stratospheric cooling near the years of 1995–2000 (the specific inflection point might vary with region) (*10*, *12*, *13*, *35*), while tropospheric temperature keeps rising (*14*, *21*). The link between $H$ and $T_{STR}$ is generally weaker if the analysis period encompasses the inflection point of stratospheric temperature.

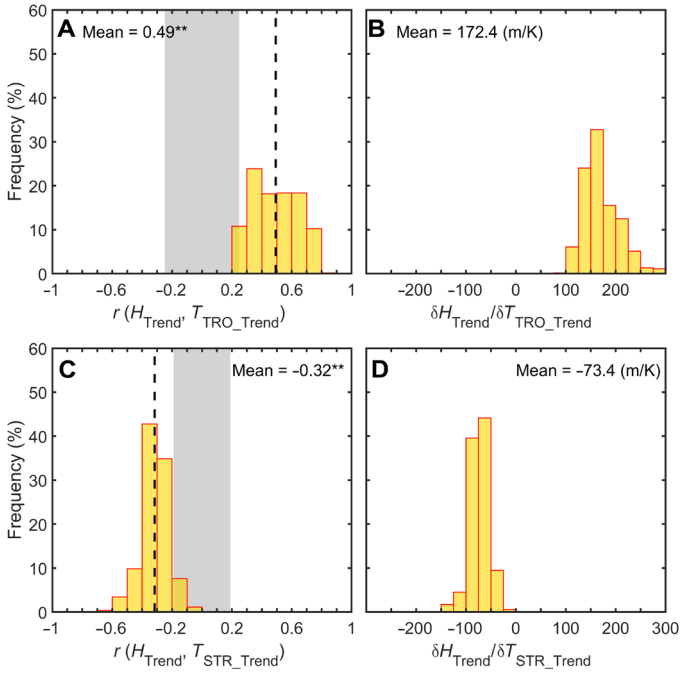


**Fig. 3. Histograms of correlation and regression slope between trends of *H* and $T_{TRO}$ and between trends of *H* and $T_{STR}$.** Histograms of the correlation coefficients ($r$) between derived trends of $H$ and $T_{TRO}$ (**A**) and $T_{STR}$ (**C**) in the NH over 1980–2020. Each $r$ is a correlation coefficient between the trends in the two corresponding variables (e.g., the trend of $H$ versus the trend of $T_{TRO}$) across the 149 stations over a specified period. All possible periods between 1980 and 2020 longer than 10 years are considered; thus, periods are between 10 and 41 years, and this results in 528 sample values of $r$. The mean $r$, shown in text and by the vertical dashed line, is significant at the 95% confidence level, indicated by double asterisks. The gray shaded areas indicate the "null hypothesis" regions for the confidence level, which is determined with consideration of autocorrelation. The corresponding regression coefficients between the trends of $H$ and $T_{TRO}$ (**B**) and $T_{STR}$ (**D**) are also shown, which are determined from a multiple linear regression model that takes the trends of $T_{TRO}$ and $T_{STR}$ as two predictors for the trend of $H$.

Quantitatively, by applying a multiple linear regression model and using $T_{TRO}$ and $T_{STR}$ trends as two predictors for the $H$ trend (see Materials and Methods), the mean response of decadal trends in $H$ is estimated to be 172 m/K to $T_{TRO}$ (Fig. 3B) and −73 m/K to $T_{STR}$ (Fig. 3D) in the NH over 1980–2020, demonstrating a larger response in $H$ to the variation in $T_{TRO}$ than to that in $T_{STR}$. Although this is the case over 1980–2020 and the two subperiods (table S2), there are differences in the regression coefficient between trends of $H$ and $T_{TRO}$ (or $T_{STR}$) among different periods, indicating that the quantitative response of $H$ to the change in $T_{TRO}$ or $T_{STR}$ is influenced by the evolution of long-term trends in $T_{TRO}$ and $T_{STR}$.

## The relative importance of tropospheric warming and stratospheric cooling to *H* rising

Analyzing the long-term trends of $T_{TRO}$ and $T_{STR}$ is useful for assessing their roles in modulating the trend in $H$. Over 1980–2000, the IGRA2 radiosonde data show that the mean $T_{TRO}$ rises at 0.17 ± 0.03 K/decade (Fig. 4A), while $T_{STR}$ decreases at −0.58 ± 0.05 K/decade (Fig. 4B). After 2000, warming of $T_{TRO}$ is amplified with a rate of 0.31 ± 0.02 K/decade, while cooling of $T_{STR}$ slows down with a rate of −0.14 ± 0.04 K/decade (Fig. 4). As discussed, tropospheric warming is associated with increasing GHGs, while stratospheric cooling is associated with both stratospheric ozone depletion and increasing GHGs. After the late 1990s, partial recovery of stratospheric ozone has been observed from satellite and ozonesonde data in both NH and SH (*36*–*38*). The ozone assessment by the World Meteorological Organization (WMO) (*39*) stated that "outside the polar regions, upper stratospheric ozone has increased by 1–3% per decade since 2000." Total column ozone from satellite observations has stabilized since the late 1990s (*40*). The enhanced rate of tropospheric warming and reduced rate of stratospheric cooling after 2000 are further illustrated in fig. S3 (B and C) (long-term evolution) and in fig. S5 (spatial variations). The slowdown in tropospheric warming over the period 2002–2013 was strongly influenced by weak low-latitude temperature trends (*17*), pointing to a driver at low latitudes such as Pacific variability (*15*, *18*). After weaker warming in the early 2000s, temperature increased during the development of El Niño conditions in 2014–2016 (*20*). The present acceleration of tropospheric warming after 2014 results from further continuous increase in GHG emissions and internal climate variability, with the onset of a positive phase of the IPO in 2014 (*19*), which represents ENSO-like variations on an interdecadal scale (*41*). Overall, the warming rate of $T_{TRO}$ has increased since 2001 compared with the earlier decades (*14*), which is associated with increases in sea surface temperatures (*21*). Comparing the $T_{TRO}$ trends between the original and natural variability–removed time series over 2001–2014, we found that the trend is 0.09 ±

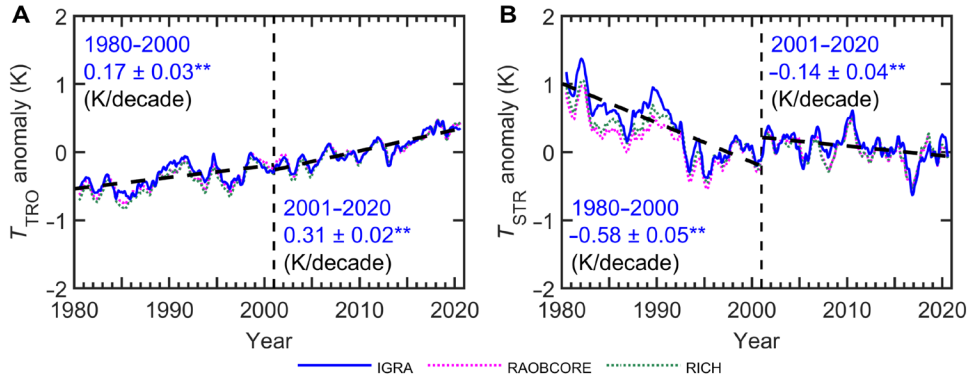


**Fig. 4. Time series of tropospheric temperature ($T_{TRO}$) and lower stratospheric temperature ($T_{STR}$) in the NH over the time period 1980–2020.** As in Fig. 1A, the solid blue, dashed purple, and dashed green lines show the time series of ($T_{TRO}$) (**A**) and ($T_{STR}$) (**B**) from the radiosonde IGRA2, RAOBCORE, and RICH data, respectively, smoothed with an 11-month running mean, while the dashed thick black lines denote the linear trends in IGRA2 over the indicated periods. The linear trends in IGRA2, denoted in the text, are all statistically significant at the 95% confidence level (indicated by double asterisks). The linear trends in RAOBCORE and RICH are listed in Table 1A. In the time series, the effects of volcanic eruptions, ENSO, and QBO have been statistically removed.

0.04 K/decade for the former and 0.21 ± 0.04 K/decade for the latter, indicating the importance of ENSO to suppressing tropospheric warming over 2001–2014. We further compare $T_{TRO}$ and $T_{STR}$ in IGRA2 with those in RAOBCORE and RICH. In terms of magnitude, interannual variation, and trend (Fig. 4 and Table 1), $T_{TRO}$ and $T_{STR}$ in RAOBCORE and RICH are highly consistent with those in IGRA2 with minor differences. For example, over 1980–2000, the magnitude of $T_{STR}$ cooling trend is lower in RAOBCORE and RICH than in IGRA2 (Fig. 4B and Table 1).

Over 1980–2000, both tropospheric warming and stratospheric cooling cause $H$ to rise. In comparison, over 2001–2020, the trend in tropospheric warming increases, while the trend in stratospheric cooling subsided (Fig. 4). As the trends in $H$ for the two subperiods are comparable, we infer that after 2000, the effect of stratospheric cooling on rising $H$ is reduced, which is compensated by the enhanced effect of tropospheric warming on rising $H$. Therefore, tropospheric warming plays a larger role in elevating $H$ over 2001–2020 than over 1980–2000. To further evaluate the contributions of these two factors to $H$ rise, we combine the response rate of $H$ to the variations in $T_{TRO}$ and $T_{STR}$ (table S2) and the trends of $T_{TRO}$ and $T_{STR}$ (Table 1A) and thus estimate that the changes in $T_{TRO}$ and $T_{STR}$ over 2001–2020 contributed to $H$ rise at rates of 54 ± 3 and 14 ± 4 m/decade, respectively. In terms of fractional contribution, the variations in $T_{TRO}$ and $T_{STR}$ contribute 79 and 21% to $H$ rise, if we ignore other minor contributing factors discussed by Santer *et al.* (*4*). In comparison, over 1980–2000, using the relevant numbers in Table 1A and table S2, the corresponding contributions of $T_{TRO}$ and $T_{STR}$ are estimated to be 32 ± 6 and 31 ± 3 m/decade, equivalent to fractional contributions of 51 and 49%, respectively. Therefore, the contributions of $T_{TRO}$ and $T_{STR}$ to $H$ rise are comparable before the inflection point around 1995–2000, while $H$ rise after 2000 is primarily due to tropospheric warming.

## DISCUSSION

Both the trend analysis (Figs. 1 and 4) and correlation analysis on monthly and multidecadal scales (Figs. 2 and 3) indicate that under a combined influence of the continuous increase in GHG emissions and partial recovery of stratospheric ozone, the $H$ rise in the NH since 2000 is mainly attributable to the warming of the troposphere. The role that tropospheric warming plays in elevating $H$ in the NH dominates over 2001–2020 in both the original and natural variability–removed time series of the radiosonde data. Overall, $H$ in the NH is more sensitive to the temperature variability in the troposphere than in the stratosphere (Fig. 3). These conclusions appear robust as the trends in $H$ and those in $T_{TRO}$ (or $T_{STR}$) are correlated at highly significant levels based on large samples over multiple decades. This study uses recently updated radiosonde observations, combined with GPS RO satellite observations and homogenized radiosonde data, to reveal a clear long-term trend in $H$ in the NH over 20°N to 80°N. After major natural variability is removed, a continuous rise trend in $H$ remains. This provides an important piece of observational evidence for anthropogenic climate change.

## MATERIALS AND METHODS

### Data and trend calculations

IGRA is the largest and most comprehensive global radiosonde dataset (*24*, *42*). We used IGRA2 (*24*) with data from the 149 stations listed in table S1. The selection criteria for these stations are based on the length and completeness of their sounding records over 1980–2020 (the details are provided later). Stations with sufficient observations are mostly located from 20°N to 80°N over land (fig. S1). Tropopause height ($H$) was determined based on the WMO lapse-rate tropopause definition (*43*). We adopted the method of Zängl and Hoinka (*44*) to determine $H$ from the geopotential height and temperature profiles in each of the radiosonde records. Individual soundings, which have different vertical resolutions, were linearly interpolated to a 200-m vertical grid before tropopause identification. For each sounding at a given station, the calculated $H$ is valid only if (i) $H$ is between 5 and 18 km, (ii) the sounding extends at least 2 km above $H$, and (iii) $H$ is within a range of ±2 SDs of the 1980–2020 mean $H$ at that station.

Considering that the tropopause has some diurnal variation, and radiosonde data are usually available for the standard hours (0000 and 1200 UT), we calculated the daily mean $H$ if the data are available at both 0000 and 1200 UT. If the observational time is not at

the standard hours, we treated the soundings between 2100 and 0300 UT as soundings at 0000 UT and between 0900 and 1500 UT as soundings at 1200 UTC. The monthly mean of $H$ was calculated for a month if the daily means of $H$ were available on at least 15 days in that month. If more than 30% of the stations have no monthly mean for a given month, the monthly mean for the entire NH is treated as missing data, which is the case for less than 2% of all months in the entire time series. The trend analysis was based on the time series of monthly anomalies of $H$, in which the monthly anomaly in each month was computed by subtracting the climatological monthly mean $H$ in the corresponding month from the monthly mean $H$.

We also extracted temperature from each of the selected soundings at the surface and at 14 pressure levels including 925, 850, 700, 500, 400, 300, 250, 200, 150, 100, 70, 50, 30, and 20 hPa. Daily means, monthly means, and monthly anomalies at these pressure levels were calculated following the same procedure as for $H$. Tropospheric temperature ($T_{TRO}$) is represented by the mean of temperature at 850, 700, 500, 400, and 300 hPa, while lower stratospheric temperature ($T_{STR}$) is represented by the mean of temperature at 100 and 70 hPa. If any monthly value is unavailable at one of the corresponding pressure levels, $T_{TRO}$ (or $T_{STR}$) in that month was treated as missing data.

While the IGRA2 radiosonde data provide a long-term historical record for climatic studies of tropopause height, temporal inhomogeneity in raw radiosonde data might cause biases in time series of tropopause height and affect trend analysis. Therefore, we also examined the homogenized radiosonde observations from the RAOBCORE and RICH data [version 1.7; (*26*, *27*)]. The version of the RICH data used is RICH-obs. To identify the break points, the RAOBCORE data use background forecasts from the 40-year European Centre for Medium-Range Weather Forecasts (ECMWF) reanalysis [ERA-40, 1958–1978; (*45*)] and the interim ECMWF reanalysis [ERA-Interim, 1979 to date; (*46*)] as references, while for the RICH-obs (shorted as RICH) data, the breaks are detected by comparing to reference series generated from neighboring radiosonde series. Over 1980–2020, gridded monthly means of temperature at 13 pressure levels (850, 700, 500, 400, 300, 200, 150, 100, 70, 50, 30, 20, and 10 hPa) with a horizontal resolution of 10° × 10° are provided by RAOBCORE and RICH.

According to the method introduced by Reichler *et al.* (*47*), we computed the monthly mean of tropopause pressure based on monthly means of temperature profiles provided by RAOBCORE and RICH. Using the hydrostatic approximation and the gas equation, we converted tropopause pressure to tropopause height in virtue of monthly means of geopotential height and temperature at 37 pressure levels (from 1000 to 1 hPa), which is obtained from the fifth-generation ECMWF reanalysis (ERA5) data (*48*). The selection criteria for the available grids are similar to those for the IGRA2 stations (the details are provided later). Similarly, the monthly means of $T_{TRO}$ and $T_{STR}$ were calculated.

The satellite-based GPS RO data have provided continuous temperature and pressure measurements as a function of height in the upper troposphere and lower stratosphere with high accuracy, high vertical resolution, and global coverage since 2001 (*49*–*51*). We used the latest Wegener Center (WEGC) multisatellite GPS RO data, OPSv5.6, available from May 2001 to December 2020. WEGC OPSv5.6 provides global upper-air satellite data in high quality from multiple RO satellite missions (including CHAMP, GRACE, SAC-C, Formosat-3/COSMIC, and Metop) (*25*, *52*) and thus is widely used for climate studies (*14*, *53*, *54*). $H$ was estimated from each temperature profile following the WMO lapse-rate tropopause definition (*55*). Monthly zonal-mean $H$ data are extracted at 5° latitudinal intervals between 80°S and 80°N. The monthly anomaly for a month in each of 5° zones was computed as the difference between the monthly mean $H$ in that month and the corresponding climatological monthly mean $H$ over 2001–2020 in that zone. Note that, for a better comparison between the radiosonde (including IGRA2, RAOBCORE, and RICH) and GPS RO data, we used the mean of $H$ over 2001–2020, instead of the mean $H$ over 1980–2020, to compute monthly anomalies of radiosonde $H$ in Fig. 1. To be consistent with $H$ anomalies for investigation of $H$ responses to the changes in $T_{TRO}$ and $T_{STR}$, the same treatment was applied to $T_{TRO}$ and $T_{STR}$ in Fig. 4. However, in Figs. 2 and 3 where only the IGRA2 radiosonde data are involved, monthly anomalies of $H$, $T_{TRO}$, and $T_{STR}$ were calculated based on the corresponding climatological means over 1980–2020.

Volcanic eruptions, ENSO, and QBO are important natural phenomena that affect interannual variability of the tropopause (*49*, *56*), as well as atmospheric temperature in the troposphere and lower stratosphere (*53*, *57*–*59*). As our focus is on the tropopause trend induced by anthropogenic forcing, we removed these three natural influences from the original time series (fig. S2) before doing the trend analysis. This was done by applying multiple linear regression on the monthly anomalies of the relevant properties (i.e., $H$, $T_{TRO}$, and $T_{STR}$) at each of the radiosonde stations for the IGRA2 data, at each of the grids for the RAOBCORE and RICH data, and in each of the zonal bands for the GPS RO data (the details are provided later).

In comparison with the GPS RO data, monthly anomalies in each of 5° latitudinal zones for the IGRA2 data over 20°N to 80°N were calculated by averaging the $H$ anomalies at all stations falling into the corresponding zone. Monthly 10°-zonal anomalies were calculated as the cosine-weighted averages of zonal anomalies in the two subordinate 5° latitudinal zones. Monthly anomalies in each of 10° zones for the RAOBCORE and RICH data were calculated by averaging the $H$ anomalies at all available 10° × 10° grids falling into the corresponding 10° zone. The monthly anomalies in the NH over 20°N to 80°N were calculated as the cosine-weighted averages of all the monthly 10°-zonal anomalies between 20°N and 80°N. Both averaged anomalies in the NH over 20°N to 80°N and 10°-zonal anomalies were used in the trend analysis. Before the final trend analysis, the anomalies were filtered with an 11-month running mean (the current month, the five previous months, and the five following months) to remove perturbations on smaller scales. The significance levels of trends and correlations were tested with the $F$ test and $t$ test, respectively.

Overall, the annual means of $H$ in IGRA2 and GPS RO are in very good agreement (the differences less than 100 m), while the annual means of $H$ in RAOBCORE and RICH are generally higher by 300 to 400 m.

### The selection criteria for the radiosonde stations and RAOBCORE and RICH grids

Each of the selected radiosonde stations must satisfy the following criteria:

1) At the station, the end year of the records is later than 2016 (inclusive) and the total number of soundings is larger than 10000.

2) In at least 80% of the years, the station has valid annual means of all the studied variables, including $H$; temperature at 850, 700,

500, 400, 300, 250, 200, 150, 100, and 70 hPa; and layer mean temperature of 850 to 300 and 100 to 70 hPa, over each of the two subperiods (1980–2000 and 2001–2020). An annual mean in a year is valid only if the monthly means are available in at least 8 months and every season contains at least one monthly mean in that year.

Each of the selected grids in RAOBCORE and RICH (1980–2020) must satisfy the following criteria:

In at least 80% of the years, each grid has valid annual means of all the studied variables, including $H$; temperature at 850, 700, 500, 400, 300, 200, 150, 100, and 70 hPa; and layer mean temperature of 850 to 300 and 100 to 70 hPa, over each of the two subperiods (1980–2000 and 2001–2020). An annual mean in a year is valid only if the monthly means are available in at least 8 months and every season contains at least one monthly mean in that year.

### Removal of natural variability in the original time series of the relevant variables

Volcanic eruptions, ENSO, and QBO are important natural forcings for the variations in the studied variables $H$, $T_{TRO}$, and $T_{STR}$. To remove these naturally forced variations, we applied a multiple linear regression model to fit the anomalies varying with time ($t$) over 1980–2020 at each of the stations for the IGRA2 data and each of the grids for the RAOBCORE and RICH data, and over 2001–2020 in each of the 5° zones for the GPS RO data.

The two large volcanic eruptions of El Chichón in April 1982 and Mount Pinatubo in June 1991 have complex impacts on $H$, $T_{TRO}$, and $T_{STR}$, persisting for the following 2 to 3 years. Meanwhile, El Niño events can raise tropospheric temperatures (*57*). Therefore, we first removed the volcano-related anomalies by regressing the anomalies of $H$, $T_{TRO}$, and $T_{STR}$ against a proxy time series for volcanic intensity, which is the Northern Hemispheric monthly mean stratospheric aerosol optical depth (SAOD) at 550 nm (*60*). Note that monthly anomalies of $H$, $T_{TRO}$, and $T_{STR}$ respond to large volcanoes, ENSO, and QBO with lags of various lengths (generally less than 12 months) at different stations, grids, or latitudinal zones. Therefore, lag-correlation regression analyses (*57*) were applied.

Take $H$ as an example. In step 1, for $H$ at a station, at a grid, or in a latitudinal zone, we found the time lag at which the correlation between SAOD and $H$ is the largest. Then, we regressed the monthly anomalies of $H$ against the monthly SAOD at that lag (Eqs. 1 and 2).

In step 2, we searched for the time lags giving the highest correlations between $H$ and the ENSO index, and between $H$ and the QBO proxy. Then, we made multiple regression of monthly anomalies of $H$ against the monthly ENSO index and QBO proxy at those lags (Eq. 3). In step 2, the data in the time series after the large volcanic eruptions of El Chichón (April 1982) and Mount Pinatubo (June 1991) over 3 years were ignored to avoid any confusion of these signals.

In summary, monthly anomalies of $H$ over 1980–2020 at a station in IGRA2 or at a grid in RAOBCORE or RICH or over 2001–2020 in a latitudinal zone in GPS RO were fitted to the following equations

$$A(t) = \alpha_0 + c \times \mathrm{SAOD}(t + \tau 0) + \varepsilon(t) \quad (1)$$

$$B(t) = A(t) - c \times \mathrm{SAOD}(t + \tau 0) \quad (2)$$

$$B(t) = \alpha + \beta \times \mathrm{QBO}(t + \tau 1) + \gamma \times \mathrm{ENSO}(t + \tau 2) + \delta(t) \quad (3)$$

where $\alpha_0$, $\alpha$, $c$, $\beta$, and $\gamma$ are constants. $\tau 0$, $\tau 1$, and $\tau 2$ are the time lags for SAOD, QBO, and ENSO, respectively. $A(t)$ is the original monthly anomalies. $\alpha + \delta\,(t)$ in Eq. 3 is the residual term, which represents the resultant time series of $H$ after removing the effects of volcanic eruptions, ENSO, and QBO. We used the multivariate ENSO index (*61*) to describe the ENSO variation and took the 70 hPa zonal winds at Singapore (*62*) as a QBO proxy. Following Weber *et al.* (*40*), the Northern Hemispheric monthly mean SAOD data at 550 nm were obtained from Sato *et al.* (*63*) for the period before 1990 and from Mills *et al.* (*64*) for the period over January 1990 to November 2015 for better descriptions of the two large volcanic eruptions. The SAOD data after December 2015 are unavailable.

The same procedures were followed for $T_{TRO}$ and $T_{STR}$. Because QBO-related variations in the tropospheric temperature are negligible (*21*), no QBO effect is considered in the analysis of $T_{TRO}$. Therefore, $\beta = 0$ in Eq. 3 if $A(t)$ is the time series of $T_{TRO}$ anomalies. For a better comparison between the radiosonde and GPS RO data, we separately applied the multiple linear regression model over 1980–2000 and 2001–2020 on the original radiosonde time series in Fig. 1. To be consistent, for illustrating the responses of $H$ to the changes in $T_{TRO}$ and $T_{STR}$, the same treatment was applied to $T_{TRO}$ and $T_{STR}$ in Fig. 4. The Supplementary Materials (fig. S2) shows the IGRA2 time series for $A(t)$ (pink), $B(t)$ (yellow), and $\alpha + \delta\,(t)$ (blue) for $H$, $T_{TRO,}$ and $T_{STR}$, respectively, in the NH over 20°N to 80°N when the multiple linear regression model was separately applied. Because Fig. 3 only involves the IGRA2 radiosonde data, the multiple linear regression model was applied to the entire time series over 1980–2020 in Fig. 3.

### Correlation between the trend of *H* and that of atmospheric temperature

To examine how the trend in $H$ may be related to that in $T_{TRO}$, and how the relationships may depend on the length of the data record, we statistically assessed the relationships between the two trends. For a given period, we calculated the $H$ and $T_{TRO}$ trends at each of 149 radiosonde stations in the NH and then calculated a correlation coefficient ($r$) between the two trends using the 149 pairs of the variables. As the trend estimates over any long-term period are sensitive to the start and end years of the period (*65*, *66*), we considered all possible periods of which the lengths are 10 years or longer (i.e., up to 41 years) from 1980 to 2020. This provides 528 values of $r$ between the trend in $H$ and that in $T_{TRO}$. Similarly, 528 values of $r$ between the trend in $H$ and that in $T_{STR}$ can be calculated. While this is a large number of $r$ estimates, they will be autocorrelated because of the overlapping periods of the 528 time series for each variable. To estimate the confidence level of the mean $r$, we used a bootstrap method (*34*). The actual time series of monthly anomalies from 1980 to 2020 were divided into eight segments, and each segment has 60 values for monthly anomalies (the last segment has 72 values), and thus, the autocorrelation information is retained in each of the eight segments. We resampled these segments randomly and generated a new 492-month time series. On the basis of this new time series, we repeated the same statistical procedure and obtained a new mean $r$. The correlation between the trend in $H$ and that in $T_{TRO}$ (or $T_{STR}$) presented in the new generated time series is attributable to the temporal autocorrelation effects. A distribution of the statistical mean $r$ was built up after we repeated the procedure many times. Therefore, taking the effect of autocorrelation into

account, the confidence level of the mean *r* for the actual time series was determined using the Monte Carlo method with 5000 repetitions in this study. Specifically, the confident intervals were calculated statistically based on the mean *r* from each of the 5000 repetitions and the associated SD (Fig. 3, A and C) (*34*).

To quantify response of *H* to temperature changes in the troposphere and stratosphere, we developed a multiple linear regression model for each of the 528 periods. In the model, the trends in $T_{TRO}$ and $T_{STR}$ are two predictors for the trend in *H*. The regression coefficients of the two predictors were determined from the model (Fig. 3, B and D).

## SUPPLEMENTARY MATERIALS

Supplementary material for this article is available at https://science.org/doi/10.1126/sciadv.abi8065

## REFERENCES AND NOTES


1. A. C. Boothe, C. R. Homeyer, Global large-scale stratosphere-troposphere exchange in modern reanalyses. *Atmos. Chem. Phys.* **17**, 5537–5559 (2017).
2. J. R. Holton, P. H. Haynes, M. E. McIntyre, A. R. Douglass, R. B. Rood, L. Pfister, Stratosphere-troposphere exchange. *Rev. Geophys.* **33**, 403–439 (1995).
3. W. J. Randel, D. J. Seidel, L. L. Pan, Observational characteristics of double tropopauses. *J. Geophys. Res.* **112**, D07309 (2007).
4. B. D. Santer, M. F. Wehner, T. M. L. Wigley, R. Sausen, G. A. Meehl, K. E. Taylor, C. Ammann, J. Arblaster, W. M. Washington, J. S. Boyle, W. Bruggemann, Contributions of anthropogenic and natural forcing to recent tropopause height changes. *Science* **301**, 479–483 (2003).
5. D. J. Seidel, W. J. Randel, Variability and trends in the global tropopause estimated from radiosonde data. *J. Geophys. Res.* **111**, D21101 (2006).
6. D. J. Seidel, R. J. Ross, J. K. Angell, G. C. Reid, Climatological characteristics of the tropical tropopause as revealed by radiosondes. *J. Geophys. Res.* **106**, 7857–7878 (2001).
7. B. D. Santer, R. Sausen, T. M. L. Wigley, J. S. Boyle, K. AchutaRao, C. Doutriaux, J. E. Hansen, G. A. Meehl, E. Roeckner, R. Ruedy, G. Schmidt, K. E. Taylor, Behavior of tropopause height and atmospheric temperature in models, reanalyses, and observations: Decadal changes. *J. Geophys. Res.* **108**, ACL 1-1–ACL 1-22 (2003).
8. B. D. Santer, T. M. L. Wigley, A. J. Simmons, P. W. Kallberg, G. A. Kelly, S. M. Uppala, C. Ammann, J. S. Boyle, W. Bruggemann, C. Doutriaux, M. Fiorino, C. Mears, G. A. Meehl, R. Sausen, K. E. Taylor, W. M. Washington, M. F. Wehner, F. J. Wentz, Identification of anthropogenic climate change using a second-generation reanalysis. *J. Geophys. Res.* **109**, D21104 (2004).
9. S.-W. Son, L. M. Polvani, D. W. Waugh, T. Birner, H. Akiyoshi, R. R. Garcia, A. Gettelman, D. A. Plummer, E. Rozanov, The impact of stratospheric ozone recovery on tropopause height trends. *J. Climate* **22**, 429–445 (2009).
10. A. C. Maycock, W. J. Randel, A. K. Steiner, A. Y. Karpechko, J. Christy, R. Saunders, D. W. J. Thompson, C.-Z. Zou, A. Chrysanthou, N. L. Abraham, H. Akiyoshi, A. T. Archibald, N. Butchart, M. Chipperfield, M. Dameris, M. Deushi, S. Dhomse, G. Di Genova, P. Joeckel, D. E. Kinnison, O. Kirner, F. Ladstädter, M. Michou, O. Morgenstern, F. O'Connor, L. Oman, G. Pitari, D. A. Plummer, L. E. Revell, E. Rozanov, A. Stenke, D. Visioni, Y. Yamashita, G. Zeng, Revisiting the mystery of recent stratospheric temperature trends. *Geophys. Res. Lett.* **45**, 9919–9933 (2018).
11. C. McLandress, T. G. Shepherd, A. I. Jonsson, T. von Clarmann, B. Funke, A method for merging nadir-sounding climate records, with an application to the global-mean stratospheric temperature data sets from SSU and AMSU. *Atmos. Chem. Phys.* **15**, 9271–9284 (2015).
12. R. Philipona, C. Mears, M. Fujiwara, P. Jeannet, P. Thorne, G. Bodeker, L. Haimberger, M. Hervo, C. Popp, G. Romanens, W. Steinbrecht, R. Stubi, R. Van Malderen, Radiosondes show that after decades of cooling, the lower stratosphere is now warming. *J. Geophys. Res. Atmos.* **123**, 12509–12522 (2018).
13. W. J. Randel, L. Polvani, F. Wu, D. E. Kinnison, C.-Z. Zou, C. Mears, Troposphere-stratosphere temperature trends derived from satellite data compared with ensemble simulations from WACCM. *J. Geophys. Res. Atmos.* **122**, 9651–9667 (2017).
14. A. K. Steiner, F. Ladstädter, W. J. Randel, A. C. Maycock, Q. Fu, C. Claud, H. Gleisner, L. Haimberger, S. -P. Ho, P. Keckhut, T. Leblanc, C. Mears, L. M. Polvani, B. D. Santer, T. Schmidt, V. Sofieva, R. Wing, C. -Z. Zou, Observed temperature changes in the troposphere and stratosphere from 1979 to 2018. *J. Climate* **33**, 8165–8194 (2020).
15. A. Dai, J. C. Fyfe, S.-P. Xie, X. Dai, Decadal modulation of global surface temperature by internal climate variability. *Nat. Clim. Chang.* **5**, 555–559 (2015).
16. J. C. Fyfe, G. A. Meehl, M. H. England, M. E. Mann, B. D. Santer, G. M. Flato, E. Hawkins, N. P. Gillett, S.-P. Xie, Y. Kosaka, N. C. Swart, Making sense of the early-2000s warming slowdown. *Nat. Clim. Chang.* **6**, 224–228 (2016).
17. H. Gleisner, P. Thejll, B. Christiansen, J. K. Nielsen, Recent global warming hiatus dominated by low-latitude temperature trends in surface and troposphere data. *Geophys. Res. Lett.* **42**, 510–517 (2015).
18. Y. Kosaka, S. -P. Xie, Recent global-warming hiatus tied to equatorial Pacific surface cooling. *Nature* **501**, 403–407 (2013).
19. L. Dong, M. J. McPhaden, The role of external forcing and internal variability in regulating global mean surface temperatures on decadal timescales. *Environ. Res. Lett.* **12**, 034011 (2017).
20. S. Hu, A. V. Fedorov, The extreme El Niño of 2015-2016 and the end of global warming hiatus. *Geophys. Res. Lett.* **44**, 3816–3824 (2017).
21. M. Shangguan, W. Wang, S. Jin, Variability of temperature and ozone in the upper troposphere and lower stratosphere from multi-satellite observations and reanalysis data. *Atmos. Chem. Phys.* **19**, 6659–6679 (2019).
22. R. Sausen, B. D. Santer, Use of changes in tropopause height to detect human influences on climate. *Meteorol. Z.* **12**, 131–136 (2003).
23. P. Pisoft, P. Sacha, L. M. Polvani, J. A. Añel, L. de la Torre, R. Eichinger, U. Foelsche, P. Huszar, C. Jacobi, J. Karlicky, A. Kuchar, J. Miksovsky, M. Zak, H. E. Rieder, Stratospheric contraction caused by increasing greenhouse gases. *Environ. Res. Lett.* **16**, 064038 (2021).
24. I. Durre, R. S. Vose, X. Yin, S. Applequist, J. Arnfield, Integrated Global Radiosonde Archive (IGRA) version 2, NOAA/National Centers for Environmental Information, **10**, V5X63X0Q (2016); https://doi.org/10.7289/V5X63K0Q.
25. EOPAC Team, GNSS Radio Occultation Record (OPS 5.6 2001–2020), Wegener Center, University of Graz, Austria (2021); https://doi.org/10.25364/WEGC/OPS5.6:2021.1.
26. L. Haimberger, Homogenization of radiosonde temperature time series using innovation statistics. *J. Climate* **20**, 1377–1403 (2007).
27. L. Haimberger, C. Tavolato, S. Sperka, Homogenization of the global radiosonde temperature dataset through combined comparison with reanalysis background series and neighboring stations. *J. Climate* **25**, 8108–8131 (2012).
28. E. J. Highwood, B. J. Hoskins, P. Berrisford, Properties of the Arctic tropopause. *Q. J. R. Meteorol. Soc.* **126**, 1515–1532 (2000).
29. Q. Fu, C. M. Johanson, J. M. Wallace, T. Reichler, Enhanced mid-latitude tropospheric warming in satellite measurements. *Science* **312**, 1179 (2006).
30. D. J. Seidel, W. J. Randel, Recent widening of the tropical belt: Evidence from tropopause observations. *J. Geophys. Res.* **112**, D20113 (2007).
31. P. W. Staten, J. Lu, K. M. Grise, S. M. Davis, T. Birner, Re-examining tropical expansion. *Nat. Clim. Chang.* **8**, 768–775 (2018).
32. T. Schmidt, J. Wickert, G. Beyerle, S. Heise, Global tropopause height trends estimated from GPS radio occultation data. *Geophys. Res. Lett.* **35**, L11806 (2008).
33. B. J. Hoskins, M. E. McIntyre, A. W. Robertson, On the use and significance of isentropic potential vorticity maps. *Q. J. R. Meteorol. Soc.* **111**, 877–946 (1985).
34. B. Efron, Bootstrap methods: Another look at the jackknife. *Ann. Stat.* **7**, 1–26 (1979).
35. V. Aquila, W. H. Swartz, D. W. Waugh, P. R. Colarco, S. Pawson, L. M. Polvani, R. S. Stolarski, Isolating the roles of different forcing agents in global stratospheric temperature changes using model integrations with incrementally added single forcings. *J. Geophys. Res. Atmos.* **121**, 8067–8082 (2016).
36. J. Liu, D. W. Tarasick, V. E. Fioletov, C. McLinden, T. Zhao, S. Gong, C. Sioris, J. J. Jin, G. Liu, O. Moeini, A global ozone climatology from ozone soundings via trajectory mapping: A stratospheric perspective. *Atmos. Chem. Phys.* **13**, 11441–11464 (2013).
37. E. C. Weatherhead, S. B. Andersen, The search for signs of recovery of the ozone layer. *Nature* **441**, 39–45 (2006).
38. J. R. Ziemke, S. Chandra, Development of a climate record of tropospheric and stratospheric column ozone from satellite remote sensing: Evidence of an early recovery of global stratospheric ozone. *Atmos. Chem. Phys.* **12**, 5737–5753 (2012).
39. World Meteorological Organization (WMO), Executive Summary: Scientific assessment of ozone depletion: 2018, World Meteorological Organization, Global Ozone Research and Monitoring Project—Report No. 58, 67 pp., Geneva, Switzerland.
40. M. Weber, M. Coldewey-Egbers, V. E. Fioletov, S. M. Frith, J. D. Wild, J. P. Burrows, C. S. Long, D. Loyola, Total ozone trends from 1979 to 2016 derived from five merged observational datasets—The emergence into ozone recovery. *Atmos. Chem. Phys.* **18**, 2097–2117 (2018).
41. Y. Zhang, J. M. Wallace, D. S. Battisti, ENSO-like interdecadal variability: 1900-93. *J. Climate* **10**, 1004–1020 (1997).
42. I. Durre, R. S. Vose, D. B. Wuertz, Overview of the Integrated Global Radiosonde Archive. *J. Climate* **19**, 53–68 (2006).
43. World Meteorological Organization (WMO), Meteorology—A three-dimensional science: Second session of the Commission for Aerology [WMO Bulletin IV(4), WMO, Geneva, 1957], pp. 134–138.

44. G. Zängl, K. P. Hoinka, The tropopause in the polar regions. *J. Climate* **14**, 3117–3139 (2001).
45. S. M. Uppala, P. W. Kållberg, A. J. Simmons, U. Andrae, V. Da Costa Bechtold, M. Fiorino, J. K. Gibson, J. Haseler, A. Hernandez, G. A. Kelly, X. Li, K. Onogi, S. Saarinen, N. Sokka, R. P. Allan, E. Andersson, K. Arpe, M. A. Balmaseda, A. C. M. Beljaars, L. Van De Berg, J. Bidlot, N. Bormann, S. Caires, F. Chevallier, A. Dethof, M. Dragosavac, M. Fisher, M. Fuentes, S. Hagemann, E. Hólm, B. J. Hoskins, L. Isaksen, P. A. E. M. Janssen, R. Jenne, A. P. McNally, J.-F. Mahfouf, J.-J. Morcrette, N. A. Rayner, R. W. Saunders, P. Simon, A. Sterl, K. E. Trenberth, A. Untch, D. Vasiljevic, P. Viterbo, J. Woollen, The ERA-40 re-analysis. *Q. J. R. Meteorol. Soc.* **131**, 2961–3012 (2005).
46. D. P. Dee, S. M. Uppala, A. J. Simmons, P. Berrisford, P. Poli, S. Kobayashi, U. Andrae, M. A. Balmaseda, G. Balsamo, P. Bauer, P. Bechtold, A. C. M. Beljaars, L. van de Berg, J. Bidlot, N. Bormann, C. Delsol, R. Dragani, M. Fuentes, A. J. Geer, L. Haimberger, S. B. Healy, H. Hersbach, E. Hólm, L. Isaksen, P. Kållberg, M. Köhler, M. Matricardi, A. P. McNally, B. M. Monge-Sanz, J.-J. Morcrette, B.-K. Park, C. Peubey, P. de Rosnay, C. Tavolato, J.-N. Thépaut, F. Vitart, The ERA-Interim reanalysis: Configuration and performance of the data assimilation system. *Q. J. R. Meteorol. Soc.* **137**, 553–597 (2011).
47. T. Reichler, M. Dameris, R. Sausen, Determining the tropopause height from gridded data. *Geophys. Res. Lett.* **30**, 2042 (2003).
48. H. Hersbach, B. Bell, P. Berrisford, S. Hirahara, A. Horányi, J. Muñoz-Sabater, J. Nicolas, C. Peubey, R. Radu, D. Schepers, A. Simmons, C. Soci, S. Abdalla, X. Abellan, G. Balsamo, P. Bechtold, G. Biavati, J. Bidlot, M. Bonavita, G. De Chiara, P. Dahlgren, D. Dee, M. Diamantakis, R. Dragani, J. Flemming, R. Forbes, M. Fuentes, A. Geer, L. Haimberger, S. Healy, R. J. Hogan, E. Hólm, M. Janisková, S. Keeley, P. Laloyaux, P. Lopez, C. Lupu, G. Radnoti, P. de Rosnay, I. Rozum, F. Vamborg, S. Villaume, J.-N. Thépaut, The ERA5 global reanalysis. *Q. J. R. Meteorol. Soc.* **146**, 1999–2049 (2020).
49. T. Rieckh, B. Scherllin-Pirscher, F. Ladstädter, U. Foelsche, Characteristics of tropopause parameters as observed with GPS radio occultation. *Atmos. Meas. Tech.* **7**, 3947–3958 (2014).
50. B. Scherllin-Pirscher, A. K. Steiner, R. A. Anthes, M. J. Alexander, S. P. Alexander, R. Biondi, T. Birner, J. Kim, W. J. Randel, S.-W. Son, T. Tsuda, Z. Zeng, Tropical temperature variability in the UTLS: New insights from GPS radio occultation observations. *J. Climate* **34**, 2813–2838 (2021).
51. S.-W. Son, N. F. Tandon, L. M. Polvani, The fine-scale structure of the global tropopause derived from COSMIC GPS radio occultation measurements. *J. Geophys. Res.* **116**, D20113 (2011).
52. B. Angerer, F. Ladstädter, B. Scherllin-Pirscher, M. Schwaerz, A. K. Steiner, U. Foelsche, G. Kirchengast, Quality aspects of the Wegener Center multi-satellite GPS radio occultation record OPSv5.6. *Atmos. Meas. Tech.* **10**, 4845–4863 (2017).
53. A. K. Steiner, B. C. Lackner, F. Ladstädter, B. Scherllin-Pirscher, U. Foelsche, G. Kirchengast, GPS radio occultation for climate monitoring and change detection. *Radio Sci.* **46**, RS0D24 (2011).
54. A. K. Steiner, F. Ladstädter, C. O. Ao, H. Gleisner, S.-P. Ho, D. Hunt, T. Schmidt, U. Foelsche, G. Kirchengast, Y.-H. Kuo, K. B. Lauritsen, A. J. Mannucci, J. K. Nielsen, W. Schreiner, M. Schwärz, S. Sokolovskiy, S. Syndergaard, J. Wickert, Consistency and structural uncertainty of multi-mission GPS radio occultation records. *Atmos. Meas. Tech.* **13**, 2547–2575 (2020).
55. H. Wilhelmsen, F. Ladstädter, T. Schmidt, A. K. Steiner, Double tropopauses and the tropical belt connected to ENSO. *Geophys. Res. Lett.* **47**, e2020GL089027 (2020).
56. W. J. Randel, F. Wu, D. J. Gaffen, Interannual variability of the tropical tropopause derived from radiosonde data and NCEP reanalyses. *J. Geophys. Res.* **105**, 15509–15523 (2000).
57. G. Gu, R. F. Adler, Precipitation and temperature variations on the interannual time scale: Assessing the impact of ENSO and volcanic eruptions. *J. Climate* **24**, 2258–2270 (2011).
58. B. Scherllin-Pirscher, C. Deser, S. -P. Ho, C. Chou, W. J. Randel, Y. -H. Kuo, The vertical and spatial structure of ENSO in the upper troposphere and lower stratosphere from GPS radio occultation measurements. *Geophys. Res. Lett.* **39**, L20801 (2012).
59. H. Wilhelmsen, F. Ladstädter, B. Scherllin-Pirscher, A. K. Steiner, Atmospheric QBO and ENSO indices with high vertical resolution from GNSS radio occultation temperature measurements. *Atmos. Meas. Tech.* **11**, 1333–1346 (2018).
60. J. -P. Vernier, L. W. Thomason, J. -P. Pommereau, A. Bourassa, J. Pelon, A. Garnier, A. Hauchecorne, L. Blanot, C. Trepte, D. Degenstein, F. Vargas, Major influence of tropical volcanic eruptions on the stratospheric aerosol layer during the last decade. *Geophys. Res. Lett.* **38**, L12807 (2011).
61. K. Wolter, M. S. Timlin, El Nino/Southern Oscillation behaviour since 1871 as diagnosed in an extended multivariate ENSO index (MEI.ext). *Int. J. Climatol.* **31**, 1074–1087 (2011).
62. B. Naujokat, An update of the observed quasi-biennial oscillation of the stratospheric winds over the tropics. *J. Atmos. Sci.* **43**, 1873–1877 (1986).
63. M. Sato, J. E. Hansen, M. P. McCormick, J. B. Pollack, Stratospheric aerosol optical depths, 1850–1990. *J. Geophys. Res.* **98**, 22987–22994 (1993).
64. M. J. Mills, A. Schmidt, R. Easter, S. Solomon, D. E. Kinnison, S. J. Ghan, R. R. Neely III, D. R. Marsh, A. Conley, C. G. Bardeen, A. Gettelman, Global volcanic aerosol properties derived from emissions, 1990–2014, using CESM1(WACCM). *J. Geophys. Res. Atmos.* **121**, 2332–2348 (2016).
65. B. D. Santer, S. Solomon, G. Pallotta, C. Mears, S. Po-Chedley, Q. Fu, F. Wentz, C.-Z. Zou, J. Painter, I. Cvijanovic, C. Bonfils, Comparing tropospheric warming in climate models and satellite data. *J. Climate* **30**, 373–392 (2017).
66. B. D. Santer, S. Solomon, F. J. Wentz, Q. Fu, S. Po-Chedley, C. Mears, J. F. Painter, C. Bonfils, Tropospheric warming over the past two decades. *Sci. Rep.* **7**, 2336 (2017).
67. W. J. Randel, R. R. Garcia, N. Calvo, D. Marsh, ENSO influence on zonal mean temperature and ozone in the tropical lower stratosphere. *Geophys. Res. Lett.* **36**, L15822 (2009).


**Acknowledgments:** We thank the National Oceanic and Atmospheric Administration (NOAA) National Centers for Environmental Information (NCEI) for providing the IGRA radiosonde data. We are grateful to the WEGC EOPAC team for providing the WEGC GNSS RO OPSv5.6 data. We thank the comments and suggestions from the editor and three anonymous reviewers, which greatly help us improve this paper. We also thank colleagues and friends for valuable discussions and suggestions. **Funding:** This work was funded by the Chinese Ministry of Science and Technology National Key R&D Program of China (grant nos. 2019YFA0606803 and 2016YFA0600204). The National Center for Atmospheric Research is sponsored by the U.S. National Science Foundation. This work was partially supported by the COSMIC NSF-NASA Cooperative Agreement (grant no. 1522830), by the Canadian Space Agency (grant no. 17SUSOARTO), and by the Austrian Science Fund (FWF) under research grants P27724-NBL (VERTICLIM) and W1256-G15 (Doctoral Programme Climate Change: Uncertainties, Thresholds, and Coping Strategies). **Author contributions:** J.L. and L.M. conceived the study. L.M. developed the methodology and conducted data analysis under the supervision of J.L. W.J.R. provided critical guidance and advice. A.K.S., D.W.T., and L.W. contributed significantly to the work overall. A.K.S., H.W., and L.H. provided the GPS, RICH, and RAOBCORE data and guided application and interpretation of the data. J.L. and L.M. wrote the manuscript with valuable input from all coauthors. **Competing interests:** The authors declare that they have no competing interests. **Data and materials availability:** The radiosonde observations are openly provided by the National Oceanic and Atmospheric Administration (NOAA) National Centers for Environmental Information (NCEI), available online at https://ncdc.noaa.gov/. WEGC GNSS RO OPSv5.6 data are supported by the WEGC EOPAC team and are available online (see https://doi.org/10.25364/WEGC/OPS5.6:2021.1/). RAOBCORE/RICH data were downloaded from https://srvx1.img.univie.ac.at/webdata/haimberger/v1.7/. All data needed to evaluate the conclusions in the paper are present in the paper and/or the Supplementary Materials.

Submitted 31 March 2021
Accepted 17 September 2021
Published 5 November 2021
10.1126/sciadv.abi8065